https://doi.org/10.1016/j.apenergy.2019.113712

Localised Electrochemical Impedance Spectroscopy Investigation of Polymer Electrolyte Membrane Fuel Cells using Print Circuit Board Based interference-free System

Dengcheng Liu[a]; Rui Lin[a,*]; Bowen Feng[a]; Lihang Han[a]; Yu Zhang[a]; Meng Ni[b]; Sai Wu[a];

[a]School of Automotive Studies, Tongji University, 4800 Cao'an Highway, Shanghai 201804, China

[b]Department of Building and Real Estate, The Hong Kong Polytechnic University, Hung Hom, Kowloon, Hong Kong, China

Corresponding author:

Rui Lin, Tongji University, E-mail: ruilin@tongji.edu.cn

Abstract

Polymer electrolyte membrane fuel cells are promising power sources for vehicle and other portable applications due to their high energy efficiency and zero pollution emission during operation. To improve the performance and reliability of polymer electrolyte membrane fuel cells, effective and accurate diagnostic tools are urgently needed for polymer electrolyte membrane fuel cells practical applications. Different from the previous diagnostic methods that may damage the fuel cell structure, a novel interference-free diagnostic system based on the printed circuit board is proposed in this study. Fuel cell localized electrochemical impedance spectroscopy at different current density is observed. It is found that the activation impedance near inlet decreases sharply when current density increase. In addition, it is also found the flooding problem and the mass transport problem can occur at a medium current density due to the non-uniform behavior of the

polymer electrolyte membrane fuel cells. The proposed diagnostic system is demonstrated to be an effective tool to improve efficiency and robust of polymer electrolyte membrane fuel cells.

Key Words

Polymer electrolyte membrane fuel cell; Localised electrochemical impedance spectroscopy; Print Circuit Board; Current density; Performance consistency

Highlights:

Interference-free localised electrochemical impedance spectroscopy diagnostic system

Segment gas diffusion layer does not be needed in a localised impedance measurement.

Anode inlet gas relative humidity is essential in the increase of catalyst utilisation.

The optimum reaction site shifts as the current density increases.

Cathode outlet suffers mass transport problem even at a medium current density.

Introduction

Polymer electrolyte membrane fuel cells (PEMFCs) are promising power sources for vehicles and various portable electronic applications due to their high efficiency (over 50%) and low pollution emission in operation [1]. As reactions in a fuel cell are complex and various problems often happened during operation[2], it is necessary to develop some diagnostic methods to find the problems in time and remove or avoid them[3]. Among all the diagnostic methods, the electrochemical impedance spectroscopy (EIS) is proved to be an effective in-site and off-site way to monitor the operation state of a PEMFC.

However, traditional EIS could only illustrate information for the whole cell[4]. As a PEMFC often has a large active area, the electrochemical reactions in different regions may be different[5]. For example, Amir Amirfazli et al.[6] investigated the manifold geometry effect on stack

temperature uniformity by a modelling work. It was found that the temperature distribution tended to be non-uniform while the stack became bigger. Chi-Young Jung et al. [7] also studied the temperature distribution of fuel cell with three different Nafion membranes. Their result showed that the temperature distribution tends to be more uneven when the exchange membrane is thicker.

Researchers also developed many diagnostic methods to monitor the fuel cell spatially. One of the most useful methods is the current density distribution measurement[8, 9]. The measurement can illustrate the unevenness of current density, which means the reaction in different parts is quite different[9].

But the current density distribution only shows the performance decrease (for example, the current density drops at the same voltage), so the reason for the performance decrease remains uncertain. The causes of performance decrease may be flooding[10], drying[11], or starvation[12]. That means, only with the current density distribution data, it is difficult for researchers to optimise the operating parameters to avoid these problems.

The localised electrochemical impedance spectroscopy (Local EIS) could be a solution to this issue[4]. Earlier in 2003, Brett et al.[13] has developed a local EIS system. They applied this technology in a single-channel solid oxide fuel cell. The characteristics of impedance changes in the direction of the flow channel have been observed. However, in their work, the cell was separated entirely, and all the 10 segments have an independent electric load. The system is equal to 10 individual cells arranged side by side, which is far different from the actual cell situation.

After decades of developments, multiple Local EIS solutions have been proposed. Schneider et al. [14] developed the system with segmented graphite in 2005. Gerteisen et al.[15, 16] developed a 50-channel system in 2011, and the system consisted of graphite and spring contacts.

Roduner et al.[17, 18] performed a Local EIS test for different Nafion membranes in 2012 and their system was consisted of a point-like electrode made by Pt-coated tip. Hinds et al.[19] reported a new Local EIS system in 2015. In that system, a Nafion tube salt bridge was located in the segment, and the EIS information was achieved via the tube. In their recently published work[20], the Nafion tube system was applied in a 50 cm^2 single cell.

Reshetenko TV et al.[21] studied the effect of Gas Diffusion Layer(GDL) on PEMFC performance with current density distribution and Local EIS technology. They exchanged the standard cathode GDL (25BC) with 25BA at segment 4 to introduce a GDL defect. They proved that current density distribution and Local EIS allow to detect and localise the GDL defects.

However, all the solutions above suffered from a common problem: their systems were far away from the actual fuel cell systems. For instance, in Hinds et al.'s work[20], the fuel cell contained a graphite plate with nine holes, which changed the structure of the cell. As the graphite is hydrophilic, the water produced during the reaction may gather near the holes. That means the conclusions in this work might be still away from the real application.

The Printed Circuit Board (PCB) has applied to measure the fuel cell since 1998[22]. And it has been proved as a less disturbing system for fuel cells[23]. And Schulze et al. [24] even tried to implement the Local EIS measurement using the PCB technology. However, in that pioneering work, they could not obtain accurate diagnostic results due to the immature testing system and the use of too large embedded electrodes. The effective and accurate interference-free diagnostic system is still lacking, which is extremely important to ensure efficient and reliable operation of fuel cells for practical applications.

To fill this research gap, a novel interference-free diagnostic system based on local EIS

technique was designed and evaluated. The system contained a specially designed PCB. However, the impedance of the embedded electrode was reduced[24], and the Local EIS result has become more accurate. As the defect of GDL structure has a great influence on the performance of fuel cells[25],an experiment with 2 home-made Membrane Electrode Assemblies (MEA) was performed to determine whether the Gas Diffusion Layer (GDL) should be segmented or not. After the experiment, the Local EIS system was finally designed, and the GDL is completely preserved. Finally, the Local EIS of a fuel cell with commercial MEA at different current density has been investigated. The result shows that the Local EIS system could observe the EIS of different segments and thus diagnosing possible problems in each segment. This novel system enables reliable and accurate diagnosis of fuel cells in practical operation.

Experimental

2.1 Local EIS system

The new system is developed based on the segmented current density distribution monitor system[26]. The working electrode and the working electrode sensor are specially designed and are embedded in the PCB. The schematic of the system is illustrated in Fig. 1. Two segments whose Local EIS can be measured (EIS Seg 1 and EIS Seg 2) are presented in Fig. 1. In fact, the cell has 49 (7x7) segments and each of them has the local current monitor system as was described before[26]. Local EIS can be measured in 6 segments. And the “Main part” in Fig. 1 represents the other 43 segments.

In Fig. 1, K1 is connected to the EIS test system, K2 is off, and K3 is connected to the local current monitor system. That means: Local EIS of EIS Seg 1 is being measured, and the other 48 segments’ local current density is being monitored.

Notes for Fig. 1:

1. The circuit can operate in galvanostatic mode and potentiostatic mode. In galvanostatic mode, Isig is the feedback into the control amplifier. In potentiostatic mode, the feedback is the voltage difference (Esig) between the active Sense leads and the Reference. In this work, all the experiments were performed in galvanostatic mode. With the PCB-based current density distribution monitor system[26], it is easy to know the current of the target segment. And with the current data, it is easier to determine the parameters in EIS test if the experiments are performed in galvanostatic mode.
2. The Bias DAC and PFIR (Positive Feedback IR-compensation) DAC are set using Gamry Framework.
3. The monitor BNC connectors for Isig and Esig are lightly filtered using an RLC circuit.
4. All the resistors summing voltages into the Control Amplifier input are not shown on the schematic. Their values depend on scaling factors which are too complex to discuss in this paper.
5. The electronic load is a plug-in load from Greenlight test bench. And the electronic load is completely floating against the GND potential.
6. The “Reference” means the reference electrode. It is connected to the target segment in the PCB manually. For example, when the Local EIS of EIS Seg 1 is tested, it is connected to EIS Seg 1. When the Local EIS of EIS Seg 2 is tested, it is connected to EIS Seg 2.

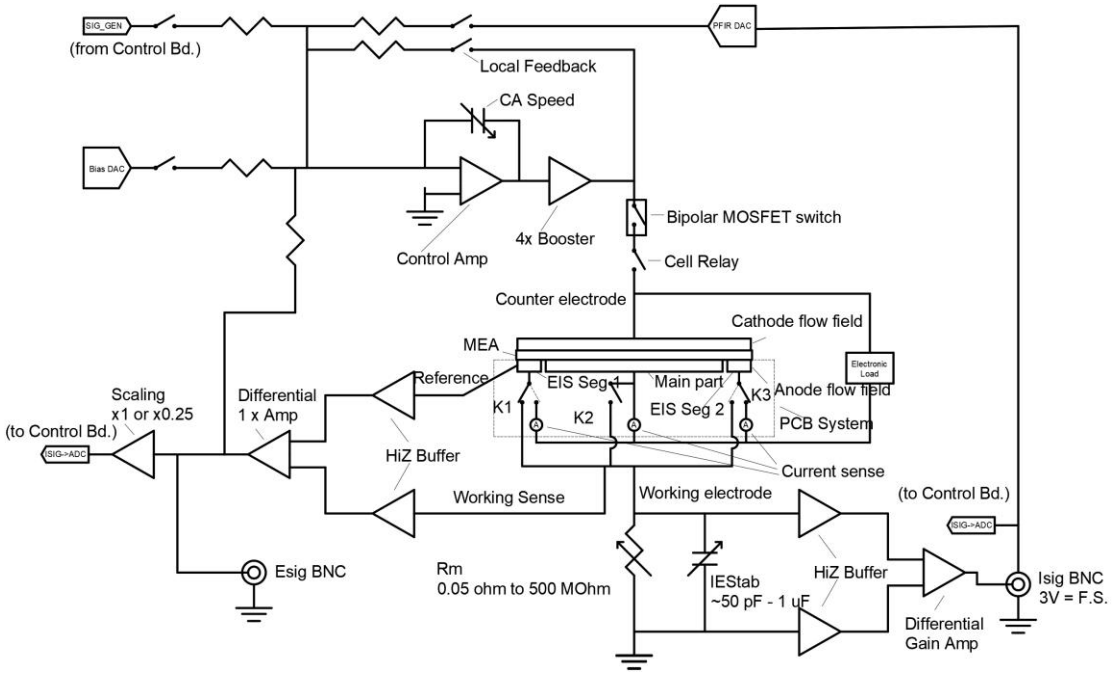

Fig. 1 The schematic of the Local EIS system (system state: K1 is connected to the EIS test system, K2 is off, and K3 is connected to the local current monitor system.)

The distribution of the segments and the anode flow field are presented in Fig. 2. The anode flow field in this paper is a three-flow serpentine channel curved on PCB. Hydrogen flows into the cell from the segment A1, which is named EIS Seg 1 in Fig. 2. Hydrogen flows out the cell from the segment G7, which is also named EIS Seg 6. On the other side, the cathode flow field is a four- flow serpentine channel curved on metal plate. Air flows into the cell from the segment G1 (EIS Seg 2) in the cathode side. Air flows out the cell from the segment A7 (EIS Seg 5) in the cathode side. The four segments above are selected as special segments to equip the Local EIS monitor system. In addition, the segment A4 and the segment G4 are also selected as special segments. The segments are defined as EIS Seg 1, EIS Seg 2, EIS Seg 3, EIS Seg 4, EIS Seg 5, and EIS Seg 6 in this paper.

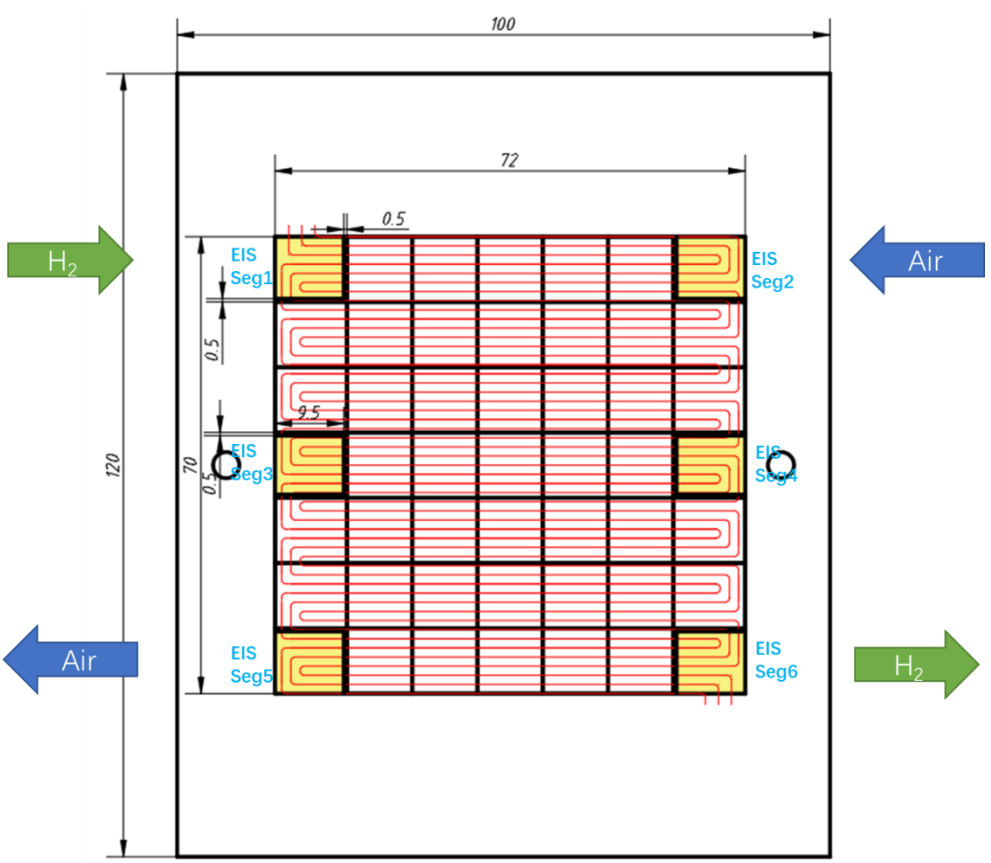

Fig. 2 Segments distribution and the anode flow field of the Local EIS system

The single cell in this work is presented in Fig. 3. The endplates in both anode and cathode are made of epoxy resin to prevent short circuits. The water flow field is composed of stainless steel and is gilded to make it anticorrosive and to have high conductivity. During the experiments, heated deionized water flows through the channel and keeps the cell at a constant temperature. The bipolar plate was also made of stainless steel and gilded.

The PCB in Fig. 3 is the part in the dotted line frame in Fig. 1 which include anode of the fuel cell, K1, K2, K3 and Current sensor. The anode flow field is carved on it. The internal circuit of PCB realizes the circuit switching of the system. Hydrogen flows into the PCB from its back

and through the flow field. Electrons generate in the anode and pass through the PCB internal circuit from 49 different segments and are collected by the water flow field.

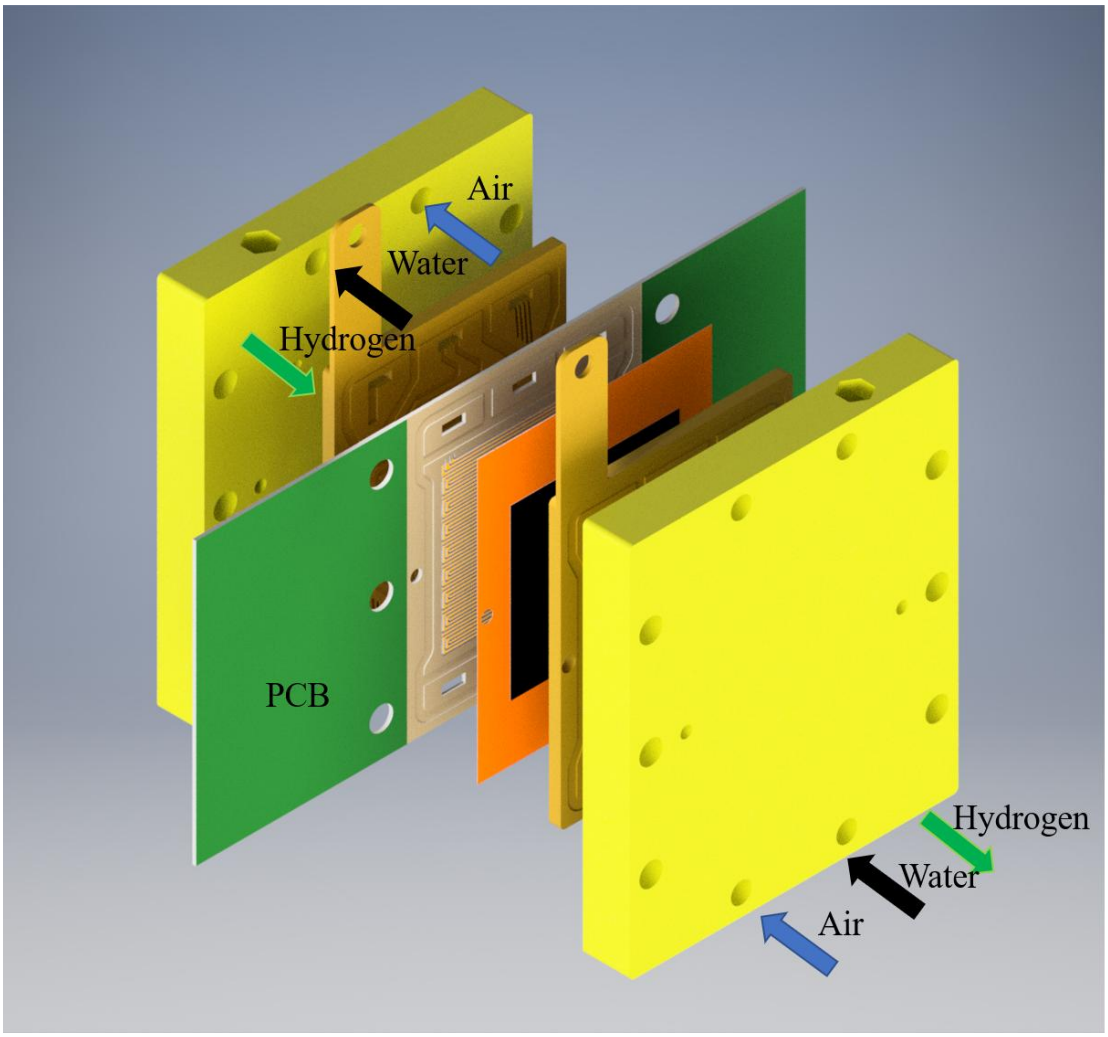

(a)

Fig. 3 The assembly exploded diagram of the fuel cell

2.2 Membrane Electrode Assemblies (MEA)

There are 3 kinds of MEAs in this work. The first one (MEA 1) is composed by Catalyst Coated Membrane (CCM) from Wuhan WUT New Energy Co., Ltd. and SGL 24BC Gas Diffusion Layer (GDL). The active area is 50 cm^2 and the overall area which contained the orange plastic paper is 120 cm^2.

The second one (MEA 2) has the same parameters with MEA 1, but the GDL on the anode side is separated into 7 parts. The 6 blocks which marked as EIS Seg 1, EIS Seg 2, EIS Seg 3, EIS Seg 4, EIS Seg 5 and EIS Seg 6 in Fig. 2, represent six smalls segmented GDL parts, and the remainder in the 70*72 mm range represents the other GDL part. The width of the cutting seam is 0.5mm as is shown in Fig. 2. As is calculated in Equ. 1, the area is 68 mm^2, only accounts for 1.36% of the total active area.

$$A_{seam} = (10 * 0.5 + 9.5 * 0.5) * 4 + (10 * 0.5 * 2 + 9 * 0.5) * 2 = 68(mm^2) \quad \text{Equ. 1}$$

MEA 1 and MEA 2 are only used to determine whether the GDL of the MEA should be segmented or not during the experiment. Local EIS studies in this work are mainly performed on a commercial one (MEA 3). MEA 3 is produced by Wuhan WUT New Energy Co., Ltd. and is the same as the former work of Lin's group[27]. Its geometry is similar to MEA 1. The details of the MEAs are shown in Table 1.

Table 1 Parameters of the MEAs

Parameter	Unit	MEA 1	MEA 2	MEA 3
Nafion membrane thickness	μm		25	
Cathode catalyst load (GM Pt/C)	$mg \cdot cm^{-2}$		0.4	
Anode catalyst load (GM Pt/C)	$mg \cdot cm^{-2}$		0.1	
GDL thickness	mm	0.235		0.17
GDL conductivity coefficient(x-y)	$W \cdot m^{-1} \cdot K^{-1}$	No data		1.7
GDL conductivity coefficient(x-z)	$W \cdot m^{-1} \cdot K^{-1}$			21
GDL area	cm^2	50 (~7.2×7.2)	49.565	50 (~7.2×7.2)
Active area	cm^2		50	

2.3 Experiments sets

All the experiments were conducted on Greenlight G20. All the EIS test, including the EIS of the fuel cell and Local EIS were performed with Gamry Reference 3000. The current density

distribution tests were conducted by the segmented cell system developed by Lin's group[28]. The High-Frequency Resistance (HFR) of the entire cell was also tested by HIOKI BT3563-01 BATTERY HITESTER.

The fuel cell working temperature was 80 ^{o}C in all the experiments. The anode stoichiometric was 1.5, and the cathode stoichiometric was 2.5. The definition of the stoichiometric is illustrated in Equ. 2. The relative humidity of the inlet gas was 75% in both anode and cathode. The backpressure was 0.3 bar during the experiments.

$$\lambda = \frac{Q_{in}}{Q_M} = \frac{u \cdot t}{M \cdot V_m / \delta} = \frac{u \cdot nF \cdot \delta}{I \cdot V_m} \quad \text{Equ. 2}$$

(where: λ is stoichiometric; Q_{in} is the actual volume of gas entering the cell; Q_M is the gas volume required for complete reaction in a certain current load; u is the gas flow rate; t is time; M is the molar of reaction gas required; V_m is the molar volume of ideal gas; δ is the gas partial pressure ratio of reaction gas; n is the number of electrons carried by a single molecule of reactive gas; F is Faraday constant; I is current.)

However, during the testing process, due to the limitation of Greenlight G20, the maximum cathode gas flow rate is 2.5 L·min^{-1}, and the maximum anode gas flow rate is 1.5 L·min^{-1}. From Equ. 2, the maximum current with a constant stoichiometric could be calculated by Equ. 3:

$$I = \frac{u \cdot nF \cdot \delta}{\lambda \cdot V_m} \quad \text{Equ. 3}$$

That means the maximum current is 56.85A. But in this work, the current load has been increased to 75A (current density was 1500 mA· cm^{-2}). At that moment, the cathode stoichiometric was only 1.89. The anode stoichiometric always kept at 1.5.

In the first experiment, Polarization curves (I-V curve) of MEA 1 and MEA 2 were achieved. The EIS of the entire fuel cell at the current density of 100 mA· cm^{-2} and 500 mA· cm^{-2} were compared. The Local EIS of EIS Seg 1 at the same current densities were also observed. After the

first experiment, EIS performance at different current densities of the fuel cell was investigated using MEA 3. EIS measurements were performed at the current density of 100 mA· cm^{-2} and were recorded every 100 mA· cm^{-2} until the current density was 1500mA· cm^{-2}. The stoichiometric at different current density is presented in Table 2. The frequency range was from 10 kHz to 1Hz, and the amplitude of a.c perturbation was set as 5% of the direct current. The amplitude values are shown in Table 2.

Table 2 The anode and cathode stoichiometric and the a.c perturbation at a different concerned current density

Current density/ mA· cm-2	Anode stoichiometric	Cathode stoichiometric	a.c perturbation/ A	Current density/ mA· cm-2	Anode stoichiometric	Cathode stoichiometric	a.c perturbation/ A
100	1.50	2.5	0.25	900	1.50	2.5	2.25
200	1.50	2.5	0.50	1000	1.50	2.5	2.50
300	1.50	2.5	0.75	1100	1.50	2.5	2.75
400	1.50	2.5	1.00	1200	1.50	2.37	3.00
500	1.50	2.5	1.25	1300	1.50	2.19	3.25
600	1.50	2.5	1.50	1400	1.50	2.03	3.50
700	1.50	2.5	1.75	1500	1.50	1.89	3.75
800	1.50	2.5	2.00				

2.4 Local EIS test

As could be observed in Fig. 1, when the EIS Segs are switched to EIS monitor system, they will disconnect with the electronic load. That means the working condition of the segment during the EIS measurement changes. However, fuel cell impedance is related to working condition. For example, when the segment is working at a high current density, the mass transport problem might be serious. If the segment is disconnected with the electronic load, the segment might be in an Open Circuit Voltage (OCV) working condition. No mass transport effect is presented in impedance measurements at OCV conditions. Impedance measurements are incorrect if they fail

to comply with Kramers-Kronig (K-K) conditions for linear, causal and stable systems.

To solve the above problems, a Direct Current Electronic Load (DCEL) is added during Local EIS test. DCEL is similar to the element in the right part in Fig. 1, but it is only connected to the EIS Seg when Local EIS is tested. The current of the segment is measured by the current density distribution monitor system. And an additional DCEL whose value is the same as the current of the segment is applied on the segment by Gamry Reference 3000. However, unlike the EIS test of the entire cell, the amplitude of a.c. perturbation during the Local EIS test was set as 10% of the local current measured by the current density distribution monitor system[29].

Fig. 4 shows an example during Local EIS test. The tested segment was EIS Seg 4 in Fig. 2. Before the segment switched to EIS test system (Fig. 4 (a)), the current density of EIS Seg 4 was 521 mA· cm^{-2}. The segment D1 had the lowest current density, which was 241 mA· cm^{-2}. The segment B2 had the highest current density, which was 679 mA· cm^{-2}.

After the switch (Fig. 4 (b)), as EIS Seg 4 was disconnected with the electronic load, the current density of EIS Seg 4 became 0 mA· cm^{-2}. Segment G3 is the nearest segment from EIS Seg 4. And the current density of G3 was 743 mA· cm^{-2} which became the highest one at that moment. Comparing with the result in Fig. 4 (a), the current density distribution was quite different, especially in EIS Seg 4 and the segments near it. If there was no DCEL added into EIS Seg 4 during the EIS test, the impedance result might be far from the desired one. The working condition of EIS Seg 4 at that time was an OCV condition.

To solve this problem, during the Local EIS measurement, DCEL was added to EIS Seg 4. As is shown in Fig. 4 (c). The current density of EIS Seg 4 recovered to 492 mA· cm^{-2}. And the current density of the segment D1 became the lowest one again, which was 251 mA· cm^{-2}. The current

density of B2 was 693 mA· cm^{-2} at that time. That means, the current density distribution was nearly the same with that in Fig. 4 (a). The current density is a sample value, and an overall scan takes five seconds. The value of EIS Seg 4 in Fig. 4 (c) consisted of alternating current and direct current. It is normal for the value ranging from 468.9 mA· cm^{-2} and 573.1 mA· cm^{-2}.

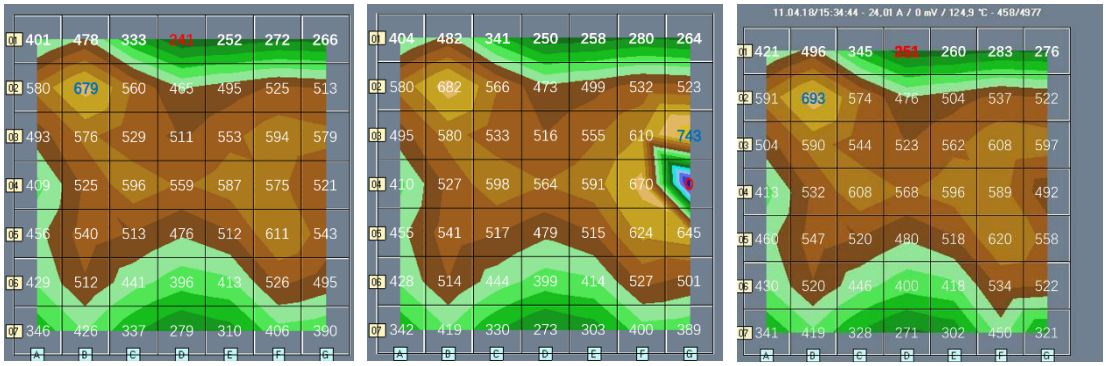

(a) (b) (c)

Fig. 4 Current densities distribution (a)before EIS Seg 4 switch to Local EIS test mode, (b)after the switch and(c) during EIS measure. Red: the smallest data; Blue: the biggest data.

Results and discussions

3.1 Comparison between MEA 1 and MEA 2

As could be observed in Fig. 5, the performance of MEA 1 and MEA 2 was quite different. MEA 1 (The red curves in Fig. 5) maintained higher voltage than that of the MEA 2 (The green curves in Fig. 5) at the same current density. The highest current density of MEA 1 was 864 mA· cm^{-2}. However, the highest current density of MEA 2 was only 637 mA· cm^{-2}, which was only 73.7% of that of MEA 1. The active area without GDL only accounts for 1.36% of the total active area. It could be concluded that if the GDL is segmented, not only the active area without GDL will

be affected, but also the other parts of the MEA will also be affected.

The output power density is obtained by Equ.3. The power density peak of MEA 1 appeared at the current density around 600 mA· cm^{-2}. The peak of MEA 2 appeared at the current density around 400 mA· cm^{-2}. As could be observed in Fig. 5, the power density peaks appeared at the voltage around 0.4V both in MEA 1 and MEA 2. In activation polarization part, the curves of MEA 1 and MEA 2 almost coincided. It could infer that the reason for the performance difference was not the catalyst activity decrease, but the Ohmic resistance increase and the mass transfer problems.

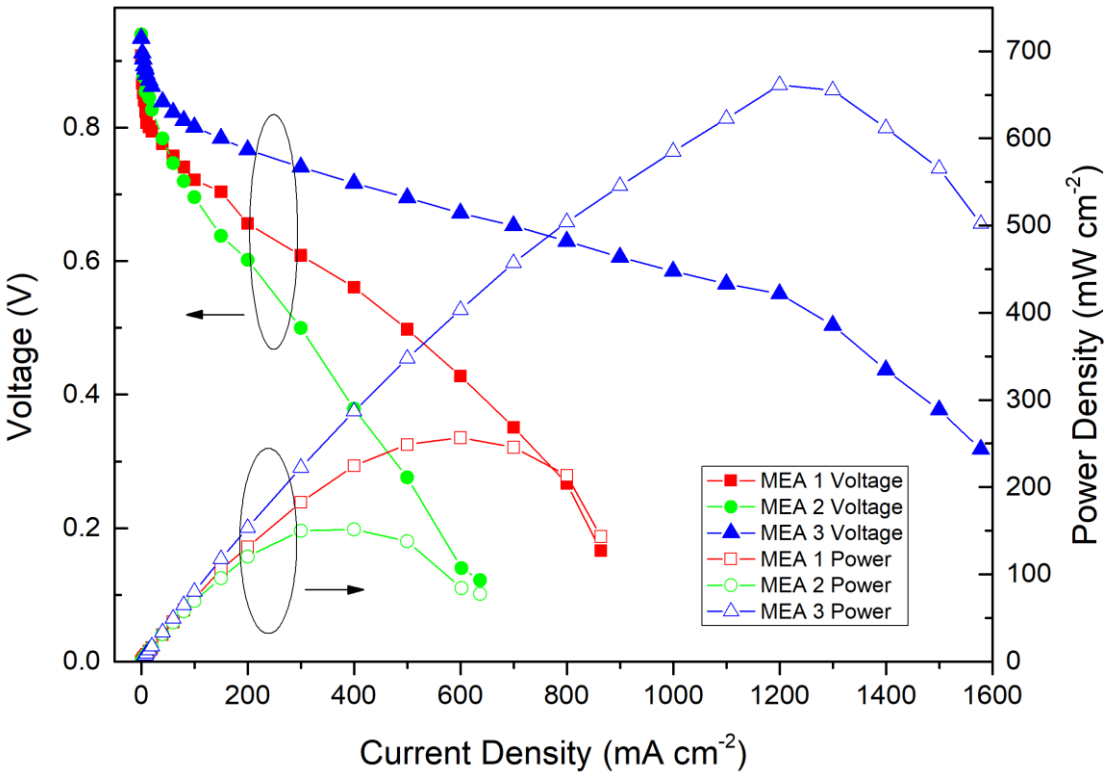

Fig. 5 Polarization curves of MEA 1 (red) MEA 2 (green) and MEA 3 (blue) (The fuel cell working temperature was 80 ^{o}C in all the experiments. The anode stoichiometric was 1.5 and the cathode stoichiometric was 2.5 (ideal), respectively. The relative humidity of the inlet gas was 75% in both anode and cathode. The backpressure was 0.3 bar during the experiments.)

$$p = U \cdot i \qquad \text{Equ. 4}$$

(Where: p is the power density; U is the voltage; and i is the current density.)

The voltage difference between these two MEAs increased with the current density increase. The voltage difference rate was obtained by Equ. 3 and increased when the current density increased. It should be noted that at a low current density, the voltage differential rate was less than 10%, and the value was within the allowable range of a test error. However, when the current density was higher than 100 mA· cm^{-2}, the voltage difference rate became bigger and bigger. It could be concluded that the output voltage performance of MEA 2 was much worse than MEA 1. A segmented MEA could not represent an unsegmented MEA, and the conclusion achieved by experiments in a segmented MEA could not be utilised in real fuel cells.

$$a = \frac{U_2 - U_1}{U_2} \qquad \text{Equ. 5}$$

(Where: a is the voltage difference rate; U_1 is the voltage of MEA 1; and U_2 is the voltage of MEA 2.)

Table 3 Voltage difference and differential rate between MEA 1 and MEA 2

Current Density/ mA· cm-2	Voltage difference/ V	Differential rate/ %	Current Density/ mA· cm-2	Voltage difference/ V	Differential rate/ %
0	-0.032	-3.524	100	0.026	3.601
2	-0.042	-4.844	150	0.066	9.375
4	-0.025	-2.934	200	0.05433	8.278
6	-0.034	-4.043	300	0.10867	17.854
8	-0.03	-3.641	400	0.182	32.442
10	-0.051	-6.312	500	0.222	44.578
15	-0.0435	-5.427	600	0.288	67.29
20	-0.032	-4.025	700	0.229	65.242
40	-0.008	-1.031	800	0.267	100
60	0.011	1.451	864	0.166	100
80	0.021	2.834			

As could be observed in Fig. 6 (a), the EIS results of the fuel cell with MEA 1 and MEA 2 was quite different. Comparing the curves at the same current density, it could be found that the HFR of the fuel cell with MEA 2 was higher than that of the fuel cell with MEA 1 no matter the current density was 100 mA· cm^{-2} or 500 mA· cm^{-2}. The radius of the Nyquist arc of the fuel cell with MEA 2 was also bigger than that of the fuel cell with MEA 1. That means the impedance of the fuel cell with MEA 2 was higher Meanwhile, it could be observed that the HFR of these two fuel cells grew with the current density increase. And the radius of the arc also became larger when the current density became higher.

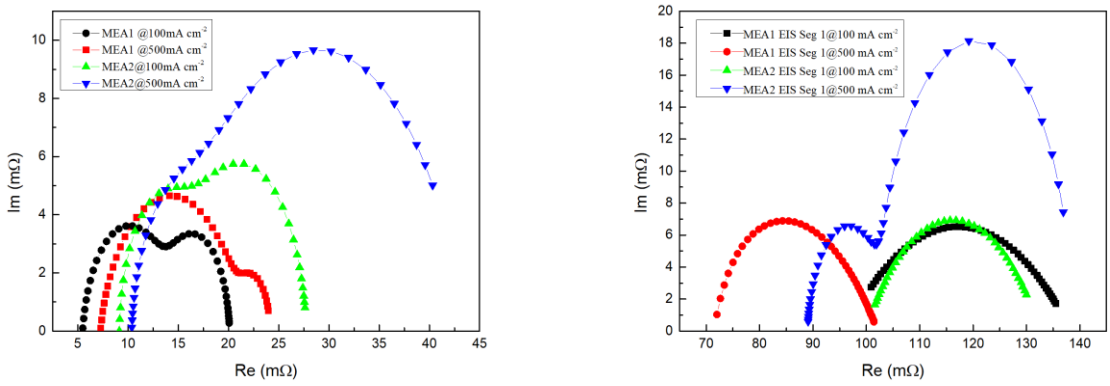

(a) (b)

Fig. 6 (a) Fuel cell EIS result and(b) Local EIS result of EIS Seg 1 at different current density. (The fuel cell working temperature was 80 °C. The anode stoichiometric was 1.5 and the cathode stoichiometric was 2.5, respectively. The relative humidity of the inlet gas was 75% in both anode and cathode. The backpressure was 0.3 bar during the experiments. The AC frequency was from 10000Hz to 1Hz)

Fig. 6 (b) shows the Local EIS of EIS Seg 1 in these two fuel cells at the same current density. Observing the black curve and the green curve in Fig. 6 (b), it could be found that the Local EIS result of EIS Seg 1 in MEA 1 and MEA 2 was almost the same. Although the HFR of these 2

results were slightly different, the height of the semi-circular arc is almost the same. The intersection of the black curve and the real axis is on the left of that of the green curve in Fig. 6 (b). It could be inferred that the HFR of the EIS Seg 1 in MEA 1 was smaller than that in MEA 2. This phenomenon is consistent with the expectation: the GDL in MEA 2 was segmented, and the area of EIS Seg 1 in MEA 2 is smaller than that in MEA 1. The Ohmic resistance takes a large part of the HFR, and the Ohmic resistance could be calculated by Equ. 6. In this work, ρ could be taken as a constant, and L here is the thickness of the GDL and could also be taken as a constant. For this reason, R is inversely proportional to S. And as the GDL in MEA 2 was segmented, the area is then smaller than that of MEA 1. So, R of EIS Seg 1 in MEA 2 is bigger than that in MEA 1.

In addition, the change of the GDL geometric could also affect the distribution of water in the cell. In Zhou Y et al's model[30], the water generated by fuel cells tends to accumulate at the deformed sites of GDL. In this work, cutting gap could be taken as a deformed site of GDL, which tends to accumulate water. The area decrease also might block the conduction of electrons that generated in the area without GDL, and the water generation might be affected. The water is conducive to the protons transport in the membrane and catalyst layer. The area decrease would also result in a decrease in the proton conduction in the catalytic layer and the membrane which increased the HFR of EIS Seg 1. This result is consistent with the results of Reshetenko TV et al.[21]. In their work, a defect in segment 4 causing the resistance raise compared with an intact GDL. In this work, cutting gap could be taken as a defect, which may increase resistance.

The height of the arc is mainly affected by the charge transfer and the mass transport. As could be seen in Fig. 5 and Table 3, the performance of MEA 1 and MEA 2 was almost the same when the current density was 100 mA· cm^{-2}. Therefore, it is reasonable for the height of the arcs is

almost the same in Fig. 6 (b). This phenomenon could also prove that the Local EIS test in MEA 1 whose GDL is unsegmented is as meaningful as that in MEA 2 whose GDL has been segmented. In another word, there is no need to cut the GDL.

$$R = \frac{\rho L}{S} \quad \text{Equ. 6}$$

(Where: R is the Ohm resistance; ρ is the resistivity; L is the length of the resistance; and S is the area.)

As is shown in Fig. 5 and Table 3, the working condition of EIS Seg 1 in the fuel cell with MEA 1 at the current density of 500 mA· cm^{-2} was different from that in the fuel cell with MEA 2. The comparison between the red and blue curve in Fig. 6 (b) may be meaningless as they were different working condition. However, the trend of impedance is worth to be studied. It could be seen that the HFR of the fuel cell with MEA 1 decreased while the fuel cell with MEA 2 increased when the current density increased. The HFR behaviour of the fuel cell with MEA 1 is the same with MEA 3(The HFR result was measured by HIOKI and was presented in Fig. 8): both decreased when the current density increase. The phenomenon could be explained by the water generated by the higher current density. As discussed above, the behaviour of the fuel cell with MEA 2 was abnormal to an uncut cell. The increase of HFR may be due to the blocked catalyst: the fuel cell was facing mass transfer problem as is shown in Fig. 5. But the HFR of EIS Seg 1 in fuel cells with MEA 1 and MEA 2 dropped when the current density increased. The HFR drop in EIS Seg 1 may be due to the increase of flow rate in anode and cathode side. When the current density increased, the flow rate increased as the stoichiometry was fixed. The higher flow rate brought more water vapor which wet the proton exchange membrane, improved the proton conductivity and reduced the HFR of the inlet (EIS Seg 1). However, in other segments, the generated water might cover the active port of the catalyst, leading to conductivity decrease. This means that the impedance of the fuel cell and

of some specific segments might be totally different. It could be concluded that studying Local EIS is meaningful for researchers to find the internal reaction mechanism and then improve the performance efficiently.

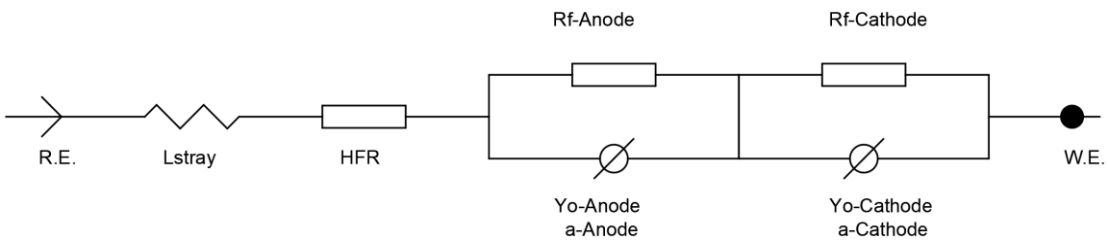

Fig. 7 Impedance data model

The EIS data in Fig. 6 is calculated by fitting Randles Model[31] by Gamry Echem Analyst software. The model is shown in Fig. 7 and the fitting result is shown in Table 4.

Table 4 Fitting result by Gamry Echem Analyst Software

parameter	Group							
	MEA1@100mA cm-2	MEA1@500mA cm-2	MEA2@100mA cm-2	MEA2@500mA cm-2	MEA1 EIS Seg 1@100mA cm-2	MEA1 EIS Seg 1@500mA cm-2	MEA2 EIS Seg1 @100mA cm-2	MEA2 EIS Seg 1@500mA cm-2
HFR/mΩ	6.824	5.186	9.036	10.22	110.8	83.41	99.77	88.98
Rf-cathode/mΩ	14.64	8.89	7.223	5.147	61.2	77.9	0.3286	13.81
Yo-cathode/S*s^a	1.331	0.6189	0.1062	0.2196	0.02863	0.06103	1479	0.07009
a-cathode	0.7186	0.8316	1	1	0.7285	0.6698	0.2171	0.9135

Rf-anode/mΩ	2.708	6.035	11.51	28.32	22.92	14.01	32.6	35.74
Yo-anode/S*s^a	116.5	10.43	1.099	2.111	1.172	1.421	1.355	0.9604
a-anode	1	0.9525	0.9214	0.7469	0.7596	1	0.5099	1
Lstray/H	7.735E-08	9.508E-08	7.246E-08	2.998E-08	3.159E-13	1.442E-08	7.491E-10	3.01E-12

3.2 HFR of the entire cell

To compare the system with others' work, HFR of the entire cell was tested using MEA 3. HIOKI BT3563-01 BATTERY HITESTER was connected to the cell and recorded HFR data. And the cell voltage gradually decreased from 0.75V to 0.45V during the test.

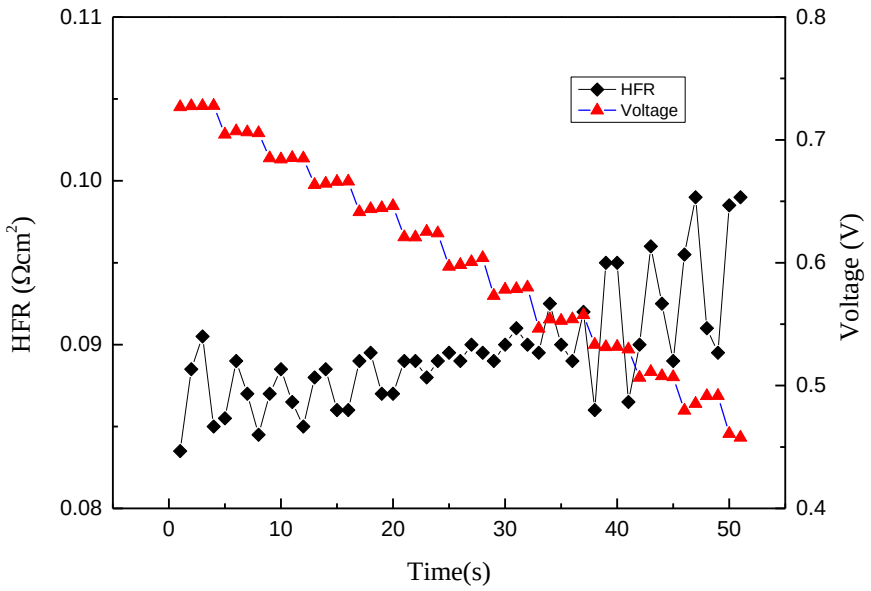

Fig. 8 HFR data of the cell, the voltage gradually decreased from 0.72V to 0.45V during the test.

As could be observed in Fig. 8, during the test, HFR increased when the voltage gradually decreased. And the value of HFR is range from 0.0835 Ωcm^2 to 0.099 Ωcm^2. Gerteisen D et al.[32] investigated HFR of their segmented PEM fuel cell at the cell voltage of 800, 700 and 500 mV, and

the average HFR was between 0.081 Ωcm^2 and 0.114 Ωcm^2. It can be concluded that the impedance of the embedded electrode in this work was smaller than their work.

3.3 Local EIS in a commercial MEA

The above experiments proved the validity and necessity of Local EIS, but the result was based on a self-made MEA whose performance is far from that of a commercial MEA. To further explore the internal reaction mechanism of fuel cells using the Local EIS technology, a commercial MEA was also used in the second part of this work.

As could be observed from Fig. 5, the performance of the commercial MEA was much better than that of the other two MEAs. The maximum current density was almost 1600 $mA \cdot cm^{-2}$. And at that current density, the voltage was still higher than 0.3V.

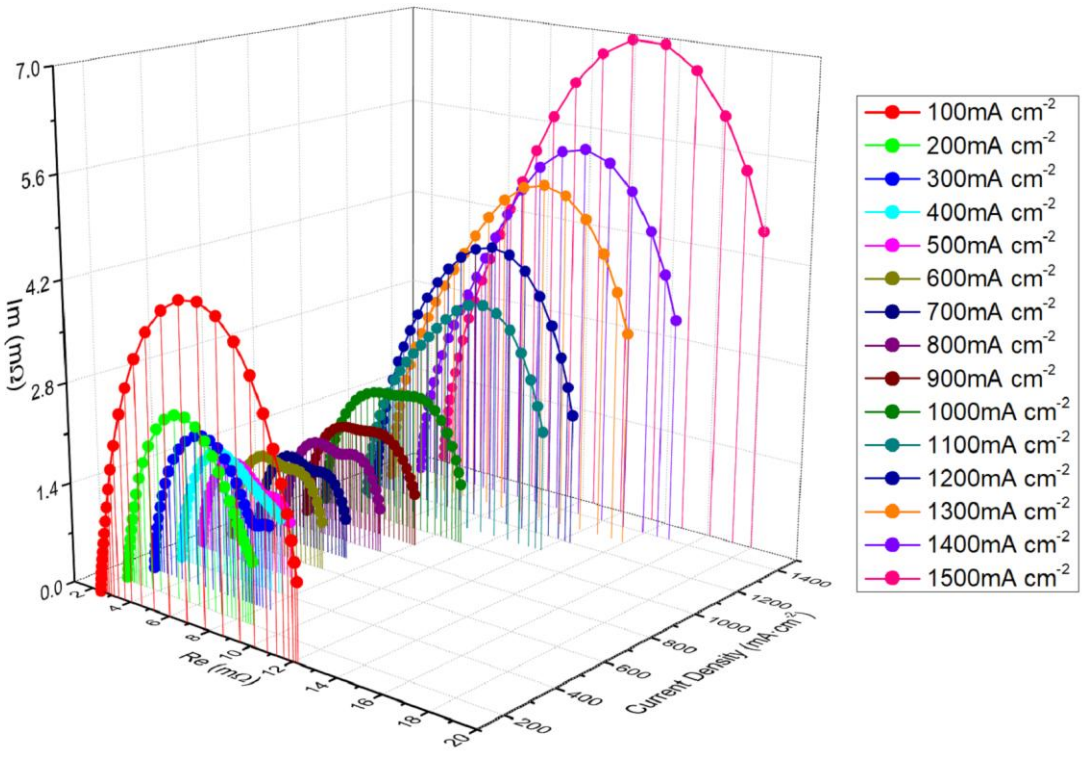

Fig. 9 EIS of MEA 3 at different current density (The fuel cell working temperature was 80 ^{o}C. The anode stoichiometric was 1.5 and the cathode stoichiometric was 2.5, respectively. The relative humidity of the inlet gas was 75% in both anode and cathode. The backpressure was 0.3 bar during the experiments. The AC frequency was from 10000Hz to 1Hz)

The 15 Nyquist Plot in Fig. 9 could be roughly classified into three types. The first type contains the curves at the current density of 100 mA· cm^{-2}, 200 mA· cm^{-2}, 300 mA· cm^{-2} and 400 mA· cm^{-2}. At this stage, the radius of the semicircle decreased with the increase of current density. The second type roughly covers the current density ranging from 500 to 900 mA· cm^{-2}. At this stage, the EIS curves basically stay unchanged with the increase of current density. The curves with a current density larger than 1000 mA· cm^{-2} could be classified into the third type. At that stage, the second semicircle became bigger and bigger with the current density increase. As mentioned in Table 2, when the current load was higher than 56.85 A (the equivalent current density is 1137 mA· cm^{-2}), the cathode stoichiometric decreased with the increase of current density. As a result, the mass transport problem became more and more obvious.

It could be observed that, at low current density, the Nyquist plots seem to consist of one semicircle. At that condition, the activation impedance may account for a large part of the overall impedance. As the current was small thus less catalyst was wetted, there was less catalyst taking part in the electrochemistry reaction. With the increase of the current density, the radius of the semicircle became smaller, which means the activation impedance was decreased. When the current density of the cell was higher than 400 mA· cm^{-2}, the radius remained almost unchanged. This phenomenon indicated that more active part of fuel cell was utilised, and the activation impedance of the fuel cells decreased with the increase of current.

The second semicircle appeared at the current density of 300 mA· cm^{-2}. It is generally accepted that the second semicircle represents the mass transfer impedance of the cell[33]. With the increase of current density, the problem of the mass transfer becomes more obvious. At the current density of 1000 mA· cm^{-2}, the second semicircle made the first semicircle invisible. This indicates that when the current density was higher than 1000 mA· cm^{-2}, the impedance of the fuel cell was mainly caused by the mass transfer problems.

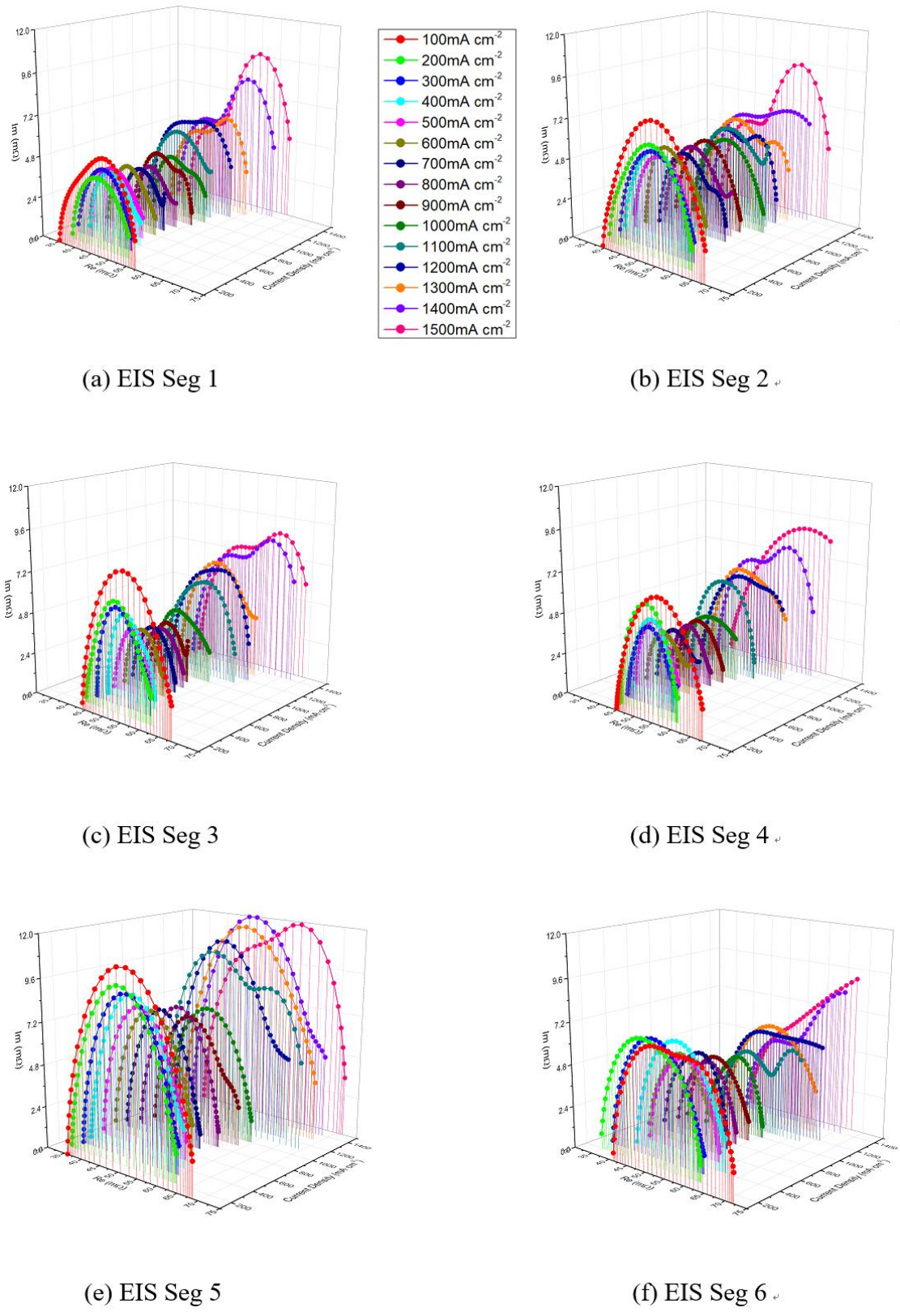

Fig. 10 Local EIS result of EIS Segs at different current density (The fuel cell working temperature was 80 ^{o}C. The anode stoichiometric was 1.5 and the cathode stoichiometric was 2.5, respectively. The relative humidity of the inlet gas was 75% in both anode

and cathode. The backpressure was 0.3 bar during the experiments. The AC frequency was from 10000Hz to 1Hz)

As could be noticed in Fig. 10, all the Local EIS Nyquist curves, which are similar to the overall EIS Nyquist curves of the cell in Fig. 9, could also be divided into three types. However, the curves of each segment had its own characteristic.

Unlike the overall fuel cell and other segments, in EIS Seg 1, although the radius of the arc at 100 mA· cm^{-2} was still bigger than that at 200 mA· cm^{-2} and 300 mA· cm^{-2}, the difference could be ignored. This implied that the catalysts in this segment were better utilised even with the lowest current load. As shown in Fig. 2, EIS Seg 1 is near the anode inlet. And in the cathode side, the flow field in EIS Seg 1 makes a U-turn. For the above reasons, it is easier to accumulate more water and wet the membrane in EIS Seg 1, thus enabling the catalyst utilised more completely. But in EIS Seg 2, a high-speed airflow (4.396 times of that in the anode side) might blow away the water contained in the membrane, which is not conducive to full utilise of the catalyst.

EIS Seg 2 is similar to EIS Seg 1. EIS Seg 2 is near the cathode inlet. And in the anode side, the flow field in EIS Seg 2 makes a U-turn. The arc radius of the Nyquist Plot in EIS Seg 2 was bigger than that in EIS Seg 1. And the difference between the curve with a current density of 100 mA· cm^{-2}, 200 mA· cm^{-2} and 300 mA· cm^{-2} was much bigger than that of EIS Seg 1. This might due to the cathode gas flow rate was significantly higher than that of the anode gas flow rate. For example, when the current density is 100 mA· cm^{-2}, the anode gas flow rate is 0.053 L·min^{-1}, and the gas flow rate in the cathode is 0.233 L·min^{-1}. Therefore, water vapor in the anode side could wet MEA along the flow path.

Combining with the current density distribution shown in Fig. 4 (a), it can be found that the

maximum current density also appears at the upper-left side of the cell, which is near the anode inlet. This validated the Local EIS data in Fig. 10. The impedance of EIS Seg 1 was also the smallest one among all the 6 segments in most situations. However, as could be observed from Fig. 10, when the current density increase, the growth rate of the impedance of EIS Seg 1 was higher than that of EIS Seg 2. That means the optimum reaction site of the cell shifted gradually from the hydrogen inlet to the air inlet with the increase of the current density.

It could be observed that the mass transport problems occurred when the current density was higher than 1100 mA· cm^{-2} in EIS Seg 1. However, in EIS Seg 2, an obvious mass transport problem occurred until a higher current density. Although the mass transport arc appeared at a current density of 1100 mA· cm^{-2}, it did not increase significantly until the current was 1400mA· cm^{-2}. This phenomenon indicated that even the cathode stoichiometric dropped, the cathode gas was still enough for the reaction near the cathode inlet. However, gas shortage occurred at the anode inlet which is not far away from the cathode inlet along the flow field. It could be concluded that a longer flow field may lead to a more serious non-uniform distribution of gas, especially at high current density.

Local EIS plots of EIS Seg 3 and EIS Seg 4 were almost the same and were similar to the whole fuel cell in Fig. 9. In Fig. 4 (a), it could be observed that the current density of EIS Seg 3 and EIS Seg 4 was the same with the entire fuel cell. It indicated that the reaction condition in EIS Seg 3 and EIS Seg 4 represented the average condition of the fuel cell. The reaction gas supply, water condition and heat exchange in EIS Seg 3 and EIS Seg 4 were almost the same with that of the entire cell. However, the first arc of EIS Seg 3 was a little bigger than that of EIS Seg 4. As is presented in Fig. 2, the path to the anode inlet of EIS Seg 3 is shorter than that of EIS Seg 4. In contrast, the

distance to the cathode inlet of EIS Seg 3 is longer than that of EIS Seg 4. From the result shown in Fig. 10 (c) and Fig. 10 (d), it could be concluded that the distance to the cathode inlet would have a great impact on the wetting effect at low current density. But when the current density increased, the difference between the two segments disappeared. As shown in Equ. 7, the reactions in fuel cells generate water. When the current density increased, more water generated in the cathode side, remedying the problem of moisture insufficient caused by the long-distance.

$$2H_2 + O_2 \rightarrow 2H_2O \qquad \text{Equ. 7}$$

As is shown in Fig. 10(e), the highest impedance at all current density appeared in EIS Seg 5. As could be recognized in Fig. 2, EIS Seg 5 located in the cathode outlet. This means the catalyst and the membrane in this segment are difficult to be wetted at low current density due to the distance from the cathode inlet. At medium current density, mass transport problems may appear earlier for the low oxygen-partial-pressure compared with the other segments. As could be observed in Fig. 10 (e), the second arc appeared at the current density of 700 mA· cm^{-2}. But in other segments, the second arc was not so obvious at the same current density. At high current density, more water generated in the cathode side, and more liquid water tended to gather in the cathode outlet. This might lead to the flooding problem in the area and this might further lead to more serious mass transport problems. As could be observed in Fig. 10(e), when the cathode flow rate was limited, the impedance increased sharply, especially when the current density is greater than 1100 mA· cm^{-2}.

Although the EIS Seg 6 is also far away from cathode and anode inlets, the impedance performance of EIS Seg 6 was better than that of EIS Seg 5. Comparing with other segments, the first type of the Nyquist Plot in EIS Seg 6 contained more curves. In other segments, the radius of the first arc in the Nyquist Plot kept almost unchanged with the current density increase after the

current density was higher than 300 mA· cm^{-2}. However, in Fig. 10(f), the radius of the first arc kept decreasing until the current density was 800 mA· cm^{-2}. This indicated that the potential of the fuel cell in the anode outlet had not been fully utilized at low current density. Considering the special location of the segment, this phenomenon is because that the anode side of the segment has not been wetted sufficiently, which results in high activation impedance.

Combining all the Local EIS results, it could be concluded that the inadequate wetting on the anode side is the main reason for the excessive activation impedance. To improve the performance at low current density, the relative humidity of the anode inlet should be increased. At high current density, insufficient gas supply will be prominent in the area not far away from the cathode inlet. To solve this problem, the gas flow rate of the cathode should be increased at high current density.

The Local EIS results also show that the cathode outlet tends to be flooding even at a medium current density. This might affect overall performance seriously. To avoid this problem, methods should be proposed to improve water management.

From the above discussion, it could conclude that the results of Local EIS technology are consistent with the local current density distribution. Moreover, Local EIS technology can discover some important information that is difficult to observe by other in-site fuel cell diagnostic methods. By using the information, methods to improve fuel cell performance can be better proposed.

Conclusions

In this work, a Printed Circuit Board-based localised electrochemical impedance spectroscopy test system was designed. The feature of the new system is interference-free to the structure of a fuel cell. During the localised electrochemical impedance spectroscopy test, a direct

current electronic load is applied to the tested segments to keep the working condition of the fuel cell the same as the condition before the test.

Two kinds of membrane electrode assemblies were placed in the system and the performance and electrochemical impedance spectroscopy were measured by the system. The performance of the segmented and unsegmented membrane electrode assembly shows that the gas diffusion layer should not be segmented in this system to have the same working condition with an actual fuel cell. The localised electrochemical impedance spectroscopy results in an unsegmented membrane electrode assembly is almost the same as the segmented membrane electrode assembly. It was concluded that the localised electrochemical impedance spectroscopy tests should be performed in an unsegmented membrane electrode assembly.

The technology was applied to observe a fuel cell with commercial membrane electrode assembly. The electrochemical impedance spectroscopy result of the total fuel cell shows that the electrochemical impedance spectroscopy results was divided into 3 types. The first type is the electrochemical impedance spectroscopy at low current density. At that stage, the cell is mainly affected by activation impedance, which decreases with the increase of current density. The second type is the electrochemical impedance spectroscopy at medium current density. At that stage, the cell is activated, and the gas supply is enough. As a result, the electrochemical impedance spectroscopy curve keeps almost unchanged when the current density increased. The third type is the electrochemical impedance spectroscopy at high current density. At that stage, the cell suffers seriously from the mass transport problems. As a result, the second arc in the Nyquist plot becomes evidently and increases with the increase of the current density.

Localised electrochemical impedance spectroscopy result shows that at low current density,

the anode inlet gas relative humidity might be the controlling factor in the fuel cell warming up process. To activate the cell as soon as possible, the relative humidity of anode gas should be increased. While at high current density, the reaction gas shortage in cathode might be very serious even when the segments are not very far away from the cathode inlet. This means that the cathode stoichiometric should be increased when the current density is high. It could be concluded that the localised electrochemical impedance spectroscopy technology can effectively improve the performance of fuel cells during operation.

Acknowledgement

The authors gratefully acknowledge financial support by the National Natural Science Foundation of China (No. 21776222) and Key Technology Research and Development Program of China (No. 2017YFB0102803) .

References

[1] Yun W, Chen KS, Mishler J, Cho SC, Adroher XC. A review of polymer electrolyte membrane fuel cells: Technology, applications, and needs on fundamental research. Applied Energy. 2011;88:981-1007.

[2] Wang J. System integration, durability and reliability of fuel cells: Challenges and solutions. Applied Energy. 2017;189:460-79.

[3] Li Z, Outbib R, Giurgea S, Hissel D, Li Y. Fault detection and isolation for Polymer Electrolyte Membrane Fuel Cell systems by analyzing cell voltage generated space. Applied Energy. 2015;148:260-72.

[4] Huang VM, Wu S-L, Orazem ME, Pébère N, Tribollet B, Vivier V. Local electrochemical impedance spectroscopy: A review and some recent developments. Electrochimica Acta.

2011.

[5] Wu HW, Shih GJ, Chen YB. Effect of operational parameters on transport and performance of a PEM fuel cell with the best protrusive gas diffusion layer arrangement. Applied Energy. 2018;220:47-58.

[6] Amirfazli A, Asghari S, Sarraf M. An investigation into the effect of manifold geometry on uniformity of temperature distribution in a PEMFC stack. Energy. 2018;145:141-51.

[7] Jung CY, Shim H-S, Koo S-M, Lee S-H, Yi S-C. Investigations of the temperature distribution in proton exchange membrane fuel cells. Applied Energy. 2012;93:733-41.

[8] Alaefour I, Karimi G, Jiao K, Li X. Measurement of current distribution in a proton exchange membrane fuel cell with various flow arrangements – A parametric study. Applied Energy. 2012;93:80-9.

[9] Lin R, Ren YS, Lin XW, Jiang ZH, Yang Z, Chang YT. Investigation of the internal behavior in segmented PEMFCs of different flow fields during cold start process. Energy. 2017;123:367-77.

[10] Li Y, Pei P, Wu Z, Peng R, Jia X, Chen D, Huang S. Approaches to avoid flooding in association with pressure drop in proton exchange membrane fuel cells. Applied Energy. 2018;224:42-51.

[11] Martin S, Garcia-Ybarra PL, Castillo JL, Martin S, Garcia-Ybarra PL, Castillo JL, Martin S, Garcia-Ybarra PL, Castillo JL. Long-term operation of a proton exchange membrane fuel cell without external humidification. Applied Energy. 2017;205:1012-20.

[12] Jia F, Guo L, Liu H. Mitigation strategies for hydrogen starvation under dynamic loading in proton exchange membrane fuel cells. Energy Conversion & Management. 2017;139:175-81.

[13] Brett DJL, Atkins S, Brandon NP, Vesovic V, Vasileiadis N, Kucernak A. Localized Impedance Measurements along a Single Channel of a Solid Polymer Fuel Cell. Electrochemical and Solid-State Letters. 2003;6:A63.

[14] Schneider IA, Kuhn H, Wokaun A, Scherer GG. Fast Locally Resolved Electrochemical Impedance Spectroscopy in Polymer Electrolyte Fuel Cells. Journal of the Electrochemical Society. 2005;152:A2092-A103.

[15] Gerteisen D, Mérida W, Kurz T, Lupotto P, Schwager M, Hebling C. Spatially Resolved Voltage, Current and Electrochemical Impedance Spectroscopy Measurements. Fuel Cells. 2011;11:339-49.

[16] Zamel N, Bhattarai A, Gerteisen D. Measurement of Spatially Resolved Impedance Spectroscopy with Local Perturbation. Fuel Cells. 2013;13:910-6.

[17] Hink S, Wagner N, Bessler WG, Roduner E. Impedance Spectroscopic Investigation of Proton Conductivity in Nafion Using Transient Electrochemical Atomic Force Microscopy (AFM). Membranes. 2012;2:237.

[18] Hink S, Roduner E. Application of a contact mode AFM for spatially resolved electrochemical impedance spectroscopy measurements of a Nafion membrane electrode assembly. Physical Chemistry Chemical Physics Pccp. 2013;15:1408.

[19] Brightman E, Chao L, Hinds G. Spatially Resolved Electrochemical Impedance Measurement in a PEM Fuel Cell Using an Array of Reference Electrodes. Journal of Power Sources. 2015.

[20] Engebretsen E, Hinds G, Meyer Q, Mason T, Brightman E, Castanheira L, Shearing PR, Brett DJL. Localised electrochemical impedance measurements of a polymer electrolyte fuel

cell using a reference electrode array to give cathode-specific measurements and examine membrane hydration dynamics. Journal of Power Sources. 2018;382:38-44.

[21] Reshetenko TV, Bender G, Bethune K, Rocheleau R. Effects of local variations of the gas diffusion layer properties on PEMFC performance using a segmented cell system. Electrochimica Acta. 2012;80:368-76.

[22] Cleghorn SJC, Derouin CR, Wilson MS, Gottesfeld S. A printed circuit board approach to measuring current distribution in a fuel cell. Journal of Applied Electrochemistry. 1998;28:663-72.

[23] Lin R, Zhu Y, Ni M, Jiang Z, Lou D, Han L, Zhong D. Consistency analysis of polymer electrolyte membrane fuel cell stack during cold start. Applied Energy. 2019;241:420-32.

[24] Schulze M, Gülzow E. Locally resolved electrochemical impedance spectroscopy of PEFC single cells. Hfc2009.

[25] Cindrella L, Kannan AM, Lin JF, Saminathan K, Ho Y, Lin CW, Wertz J. Gas diffusion layer for proton exchange membrane fuel cells—A review. Journal of Power Sources. 2009;194:146-60.

[26] Shan J, Gazdzicki P, Lin R, Schulze M, Friedrich KA. Local resolved investigation of hydrogen crossover in polymer electrolyte fuel cell. Energy. 2017;128:357-65.

[27] Liu D, Xia S, Tang H, Zhong D, Wang B, Cai X, Lin R. Parameter optimization of PEMFC stack under steady working condition using orthogonal experimental design. International Journal of Energy Research. 2018.

[28] Zhang Q, Lin R, Técher L, Cui X. Experimental study of variable operating parameters effects on overall PEMFC performance and spatial performance distribution. Energy.

2016;115:550-60.

[29] Dale NV, Mann MD, Salehfar H, Dhirde AM, Han T. ac Impedance Study of a Proton Exchange Membrane Fuel Cell Stack Under Various Loading Conditions. Journal of Fuel Cell Science and Technology. 2010;7:155-63.

[30] Zhou Y, Jiao K, Du Q, Yan Y, Li X. Gas diffusion layer deformation and its effect on the transport characteristics and performance of proton exchange membrane fuel cell. International Journal of Hydrogen Energy. 2013;38:12891-903.

[31] Fouquet N, Doulet C. Model based PEM fuel cell state-of-health monitoring via ac impedance measurements. Journal of Power Sources. 2006;159:905-13.

[32] Gerteisen D, Zamel N, Sadeler C, Geiger F, Ludwig V, Hebling C. Effect of operating conditions on current density distribution and high frequency resistance in a segmented PEM fuel cell. International Journal of Hydrogen Energy. 2012;37:7736-44.

[33] Rezaei Niya SM, Hoorfar M. Study of proton exchange membrane fuel cells using electrochemical impedance spectroscopy technique – A review. Journal of Power Sources. 2013;240:281-93.

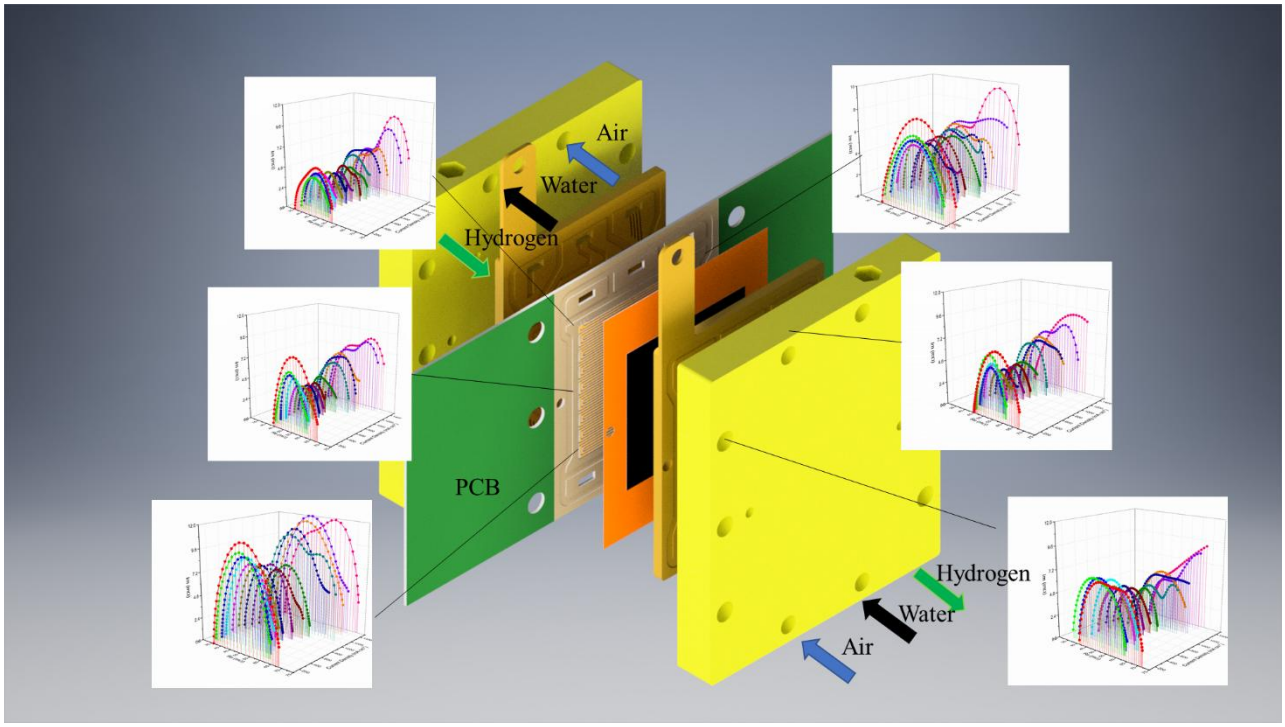

Fig.0 graphical abstract

Graphical Abstract (for review)